EARTH SURFACE PROCESSES AND LANDFORMS
Earth Surf. Process. Landforms (2010)

Published online in Wiley InterScience
(www.interscience.wiley.com) DOI: 10.1002/esp.1941

Electrical imaging of sliding geometry and fluids associated with a deep seated landslide (La Clapière, France)

H. Jomard,* T. Lebourg, Y. Guglielmi and E. Tric
Laboratoire Géosciences Azur, Universite de Nice Sophia-Antipolis (UNSA), Laboratoire Géoazur, CNRS-IRS, 250 rue A. Einstein, 06560, Valbonne, France

Received 6 November 2007; Revised 8 September 2009; Accepted 21 September 2009

*Correspondence to: H. Jomard, Laboratoire Géosciences Azur, Universite de Nice Sophia-Antipolis (UNSA), UMR 6526, 250 Av. A. Einstein, 06560 Valbonne, France. E-mail: herve.jomard@irsn.fr

ESPL
Earth Surface Processes and Landforms

ABSTRACT: This paper deals with the applicability of electrical resistivity tomography (ERT) for the recognition of large landslide structures at depths, which have never previously been imaged accurately. One of the most studied and instrumented deep landslides in Europe is taken as an example: the La Clapière landslide.

The first stage of the study consisted of an accurate geological mapping taking into account a morphological analysis of gravitational deformations. This allowed a very fine definition of the landslide structure, that could be compared with three provided ERT profiles performed within the landslide body. Very good correlations were obtained for the determination of sub-horizontal structures and associated fluid circulations. It confirmed the position of the sliding surface that reached a maximum depth of 100 m. Forward computing was however necessary to determine the influence and then the presence of vertical discontinuities. It supports the use of ERT as an efficient tool for large scale landslide imaging, such as deep seated landslides. Copyright © 2010 John Wiley & Sons, Ltd.

KEYWORDS: deep seated landslide; landslide morphology; electrical resistivity tomography (ERT); sliding surface; La Clapière landslide

Introduction

The recognition of the geometry of deep seated landslides is a fundamental stage in the understanding of mechanisms leading to wide destabilizations. As mentioned by Ferrucci *et al*. (2000), any investigation of gravitational slope deformation should include a study of the geometry of the landslide and the structure of both the landslide and the parent rock. Three types of dataset were defined by McCann and Forster (1990) for the geotechnical characterization of landslides. The determination of the three-dimensional (3D) geometry of the studied object, particularly that of the sliding surfaces; the investigation of slope hydrogeology, mainly water inputs and its pore pressure distribution within the sliding mass and finally the detection and characterization of sliding movements and rates.

Most studies on landslides combine various direct and indirect methods to assess those parameters (Bogoslowsky and Ogilvy, 1977; Caris and Van Asch, 1991; Mauritsch *et al.*, 2000; Ferrucci *et al.*, 2000; Maquaire *et al.*, 2001; Agnesi *et al.*, 2005; Bichler *et al.*, 2004; Lebourg *et al.*, 2005). The methods employed, direct or indirect are subject to operational requirements and limitations according to the studied slope conditions. Therefore it is necessary to determine the most common applicable methods for the recognition of the sliding surface in large rock-slides.

Direct recognition of the sliding surface is mainly obtained by boreholes (Hutchinson, 1983; Ayalew *et al*., 2005), but this method is seldom used for large rock slides (Forlati *et al.*, 2001) because of the high costs and the configuration of the unstable slopes, mainly linked to high internal deformation of the landslide body.

Indirect inference of landslide geometry is mainly obtained by the use of geophysical methods (Hack, 2000). Most of them are classically applied in the case of shallow and large landslides: seismic refraction (Caris and Van Asch, 1991; Mauritsch *et al.*, 2000), seismic reflection (Bruno and Marillier, 2000), self potential (Bogoslowsky and Ogilvy, 1977; Bruno and Marillier, 2000), electromagnetic imaging (Caris and Van Asch, 1991; Mauritsch *et al.*, 2000; Godio and Bottino, 2001; Bichler *et al.*, 2004), and geoelectrical imaging (Bogoslowsky and Ogilvy, 1977; Caris and Van Asch, 1991; Israil and Pachauri, 2003; Lebourg *et al.*, 2005; Jomard *et al.*, 2007a; Jomard *et al.*, 2007b; Godio *et al.*, 2006). A different indirect way to assess the sliding surface geometry was introduced by Casson *et al.* (2005), by the use of remote sensing analysis.

The necessary investigation depth to assess the sliding surface recognition of a large landslide must lie between 50 and 200 m. This considerably constrains the application of geophysical methods. In fact, only the use of seismic reflection or electrical tomography is currently possible. Seismic reflection has been the only geophysical method employed in

detection of sliding surfaces on large rock slides that has yielded results (Ferrucci *et al.*, 2000; Brueckl and Parotidis, 2001). But, the need to use explosives as the seismic source and problems of strong attenuation and the consequent high signal to noise ratio (Ferrucci *et al.*, 2000) makes that method not really suitable in the recognition of rock slide sliding surfaces geometry.

The aim of this paper is therefore to evaluate the possibility of using electrical resistivity tomography (ERT) for the characterization of large landslide structures at depth, in particular the geometry of the sliding surface.

ERT is a widely applied method to obtain two-dimensional (2D) or 3D high-resolution images of ground resistivity variations (Griffiths and Turnbull, 1985; Griffiths and Barker, 1993; Loke and Barker, 1996; Lebourg and Frappa, 2001). It has received increasing attention in recent years, in particular for shallow landslide characterization (Benderitter and Schott, 1999; Godio and Bottino, 2001; Lapenna *et al.*, 2003; Bichler *et al.*, 2004; Lebourg *et al.*, 2005). This attention is mainly linked to the efficiency of the method in detecting interstitial water in the ground (McGrath *et al.*, 2002; Garambois *et al.*, 2002; Jomard *et al.*, 2007a; Jomard *et al.*, 2007b). More recently, ERT has been successfully applied to the analysis of geologic, tectonic structures (Gourry *et al.*, 2003; Caputo *et al.*, 2003) and deeper investigations (from the kilometre to the crustal scale) highlighting discontinuities, faults, drainage channel systems, and structural features (Storz *et al.*, 2000; Colella *et al.*, 2004). This makes it possible to consider the application of this method to large rockslides.

The well known landslide of La Clapière is taken as an example (Figure 1). In spite of 25 years of monitoring and analysis of this landslide, its geometry has never been characterized in detail and

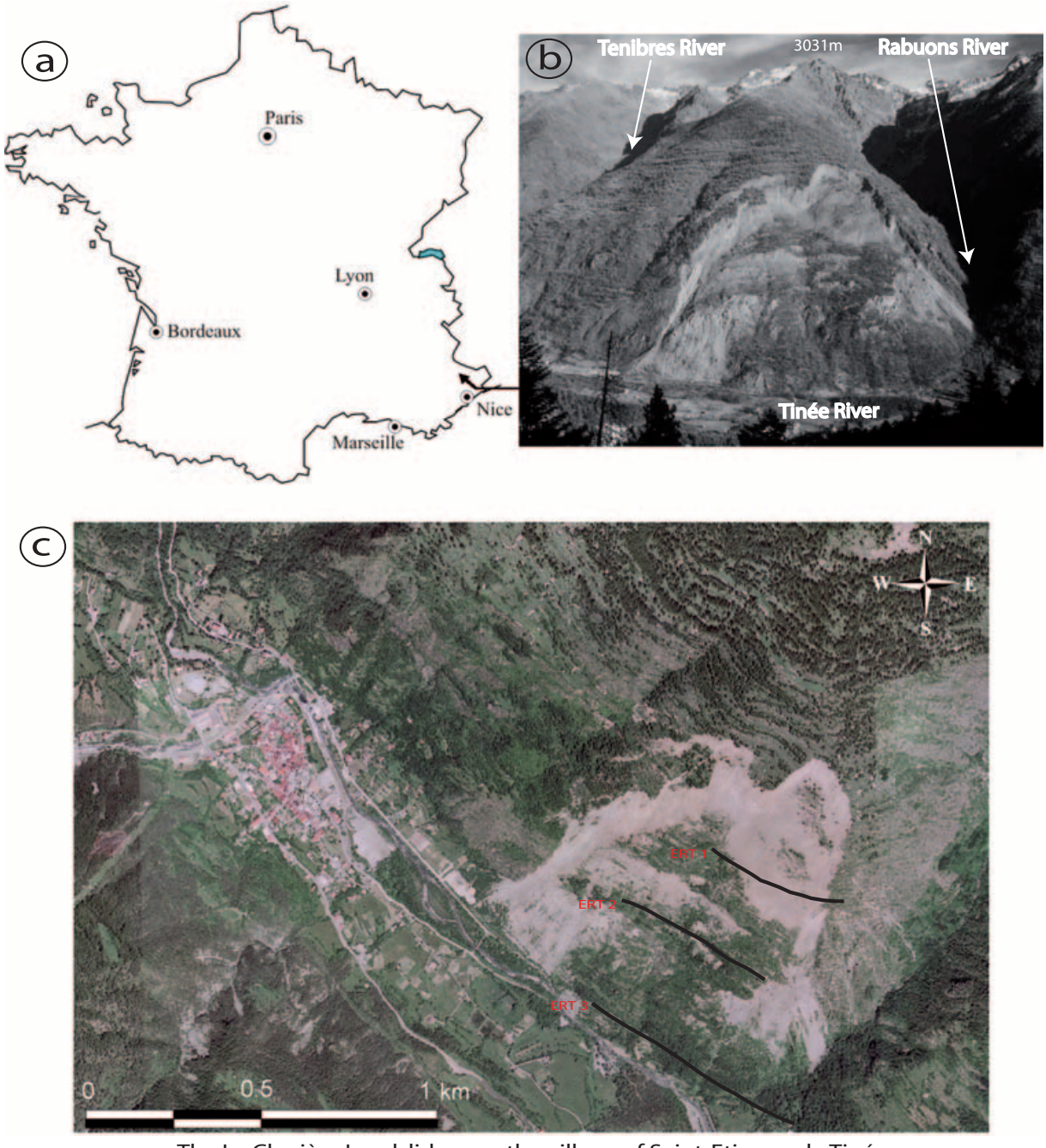

Figure 1. (a) Localization of the La Clapière landslide; (b) photograph (picture by Y. Guglielmi); (c) aerial photograph (Institut Géographique National) of the studied zone in 1999. This figure is available in colour online at www.interscience.wiley.com/journal/espl

the sliding surface has not been identified with accuracy. The calibration of the ERT method needs an accurate redefinition of the geological/hydrological structure of the landslide. The first part of this paper consists of an accurate morphologic and geologic mapping of the La Clapière slope structure. This structure will thus be compared and discussed later with three ERT acquired on the landslide body.

Geological and Geomorphological Analysis of La Clapière Landslide

Previous studies of the rock slide

The La Clapière landslide (Figure 1) is located in the French Alps, 70 km as the crow flies from the city of Nice (Figure 1a). More precisely on the left bank of the northwest (NW)–southeast (SE) oriented Tinée valley, near the village of Saint-Etienne-de-Tinée (Southern Alps, France, Figure 1c). It is bordered on its north-western side by the Tenibres River and on its south-eastern side by the Rabuons River (Figure 1b), which are fed from lakes situated at elevations of 2500 m and flow into the Tinée River. The Tinée valley elevation is 1100 m at the landslide base and the two tributaries create a 300 m deep notch of the slope. The prism culminates at an elevation of 2200 m. Elevations of surrounding crests and peaks reach 3000 m (Figure 1b). The base of the La Clapière landslide is located at the Tinée valley elevation and is 1 km wide (Figure 1c). The landslide currently overlaps the Quaternary alluvial deposits of the Tinée River. The top of the landslide is a 120 m high scarp that extends over a width of 800 m at an elevation of 1600 m.

One of the first studies of the La Clapière landslide was carried out by Follacci (1987). He interprets the current landslide as a movement included in a greater deformation zone linked to gravitational toppling of the Variscan gneisses foliation of the slope. He determines the shear surface as a circular failure affecting a column of rock 150 m thick.

Julian and Anthony (1996) further describe a mechanism which seems to be common to the whole of the Tinée valley. Its origin would be, in agreement with Follacci *et al.* (1988), that a neotectonic compression has affected alignments of the valley slopes and crests by inducing stress at the base of the hill slopes; such stress propagates upwards inducing a sliding movement as found in the La Clapière landslide. They however do not give geometrical constraints on the slip surface except the assumption of a circular shear surface ending at the foot of the slope.

Assumptions advanced until that time linked the importance of deglaciation to the initiation of a gravitational toppling which would be one of the origins of the La Clapière landslide. Gunzberger and Laumonier (2002) showed that the origin of the foliation toppling is not gravitational and that the landslide slip is not aligned on the axis of this deformation. This assumption is supported by numerical modelling (Merrien-Soukatchoff *et al.*, 2001) showing that gravity and thus the post-glacial effect cannot be at the origin of such a significant toppling.

Cappa *et al.* (2004) and Guglielmi *et al.* (2005) described this landslide as an encased slide in a fossil movement of much greater significant width and characterized by a network of trenches and fractures. The slip surface is included in a weathered bedrock zone characterized by a thickness ranging between 50 and 200 m (based on cross-section geometry). The surface is complex and structurally guided. Moreover, generated numerical models assigned columns of rocks of thickness of 150 to 200 m.

Finally, the only representation of the sliding surface of the La Clapière landslide was done by Casson *et al.* (2005) from an indirect use of remote sensing and surface deformation analysis [comparison of digital elevation models (DEMs) generated from multi-temporal stereoscopic pairs of aerial photographs]. Observations and modelling are characteristic of a non-uniform rotational behaviour of the landslide along an irregular curved slip surface located at a depth of 100 m. However, these data result from the use of important assumptions like a low internal deformation of the landslide body and give only a 2D view (transverse section) of the sliding surface.

Geostructural context

The La Clapière unstable slope is located at the north-western edge of the Argentera-Mercantour External Crystalline Massif. This basement unit consists of metamorphic rocks having recorded a polyphased tectonic and metamorphic evolution during the Variscan and Alpine orogeneses (Faure-Muret, 1947; Bogdanoff and Ploquin, 1980). The slope is composed of two-mica gneisses characterized by alternating or anastomosing thin micaceous layers, quartz-feldspar layers. A metagranodioritic layer is exposed half-way between the bottom and the top of the landslide.

The metamorphic foliation in the La Clapière zone appears undulated and microfolded. The regional metamorphic foliation in the western part of the Argentera-Mercantour strikes N130°E and dips 60° or steeper towards the northeast (NE). Close to the land surface, the foliation is horizontal or dips gently (less than 20°) either to the NE or to the southwest (SW) (Fabbri and Cappa, 2001; Gunzburger and Laumonier, 2002). In the upper part of the La Clapière slope, this toppled zone displays a N140 axial plane roughly striking to the SW. Scarps, trenches and other sagging morphological structures were observed within this uncompressed zone where metamorphic rocks are weathered on a thickness ranging from 50 to 200 m between elevations 1300 and 2200 m. A lower Triassic to Upper cretaceous sedimentary unit is identified (Faure-Muret, 1947; Malaroda *et al.*, 1970) in the right bank of the valley and covered by the Tinée alluviums. A Triassic sedimentary layer containing Gypsum underlies the La Clapière slope basement. This layer is associated with the Alpine tightly overturned syncline with an inner core of gypsum and dolomitic breccia (cargneules) enclosed by sandstone layers in the left side of the Rabuons River (Faure-Muret, 1947; Ivaldi *et al.*, 1991) and is indirectly shown by the enrichment in SO_4^{2-} of spring water originating from the landslide base (Guglielmi *et al.*, 2000). Those sediments are trapped under the gneissic basement by the Alpine displacement of the Cascaï overthrusting fault (Figures 2 and 3).

The fracture pattern of the La Clapière slope is complex. Compressive faults are represented by the Cascaï thrust that has a N130 orientation and dips to the NE (Figures 2 and Figure 3). Extensive faults are represented with two main directions (Figures 2 and 3):

- A N110–140° family dipping 60° to the SW. Faults have a 150 m average spacing that is characteristic of the overall massif. This fault set clearly characterizes the main landslide scarps (Figures 2 and 3) including the landslide head (120 m high) and the lower head dividing the landslide into a higher and a lower part.
- A N010–030° family of faults dipping 70° to 80° to the SE and the NW. Two of them contain a thick tectonic breccia (Figure 3). The north-eastern and the south-western side of the landslide are bounded by a N010 major fault (Figures 2 and 3).

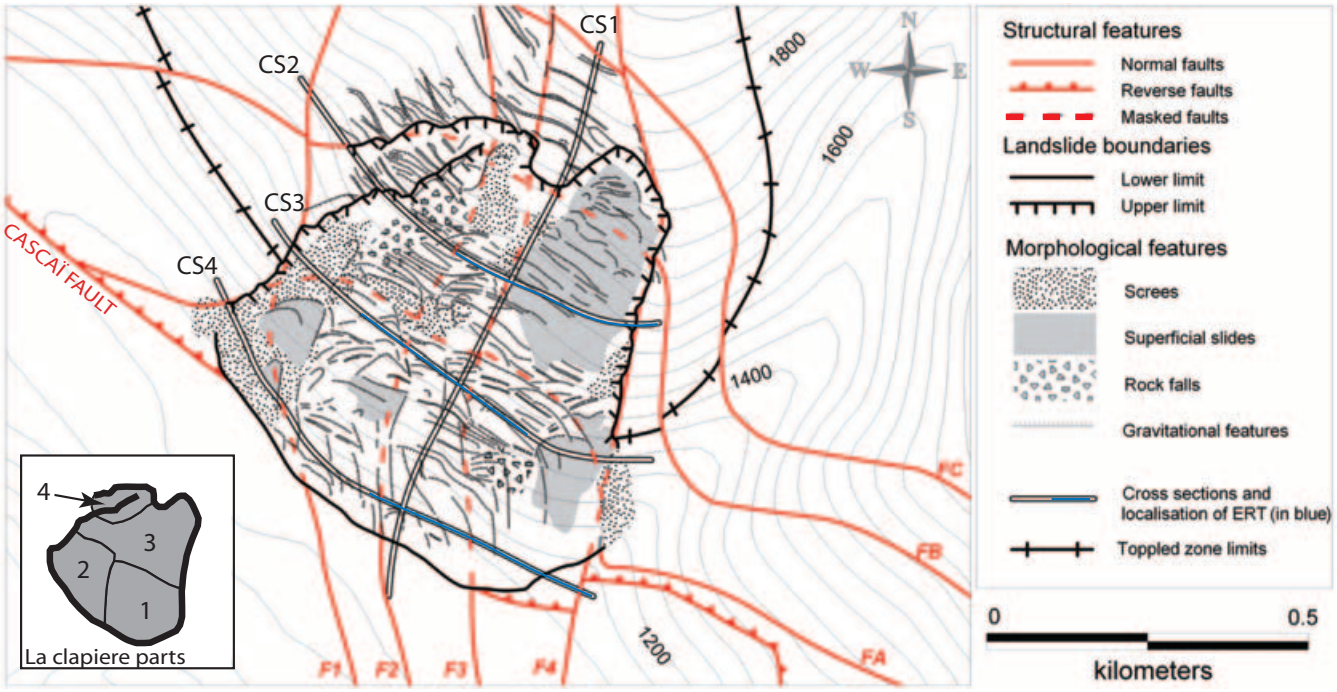

Figure 2. Morphotectonic map of the La Clapière landslide. Major superficial structures are structurally controlled dividing the landslide in four principal parts. The accurate mapping allowed the reconstruction of gravitational failure mechanisms. The three electrical profiles (ERT1–3) were respectively acquired on cross-sections CS2, CS3 and CS4. This figure is available in colour online at www.interscience.wiley.com/journal/espl

Geomorphological analyses performed to calibrate geophysical data

Detailed field work was performed to characterize the links between this tectonic pattern and the internal gravitational deformation of the sliding zone. As shown by Guglielmi *et al.* (2005), the current La Clapière landslide is only one more reactivation of larger and older slope movements corresponding to a large scale toppling. It means that the slope already had gravitational failure features before the historical failure. The current landslide started in the 1950s with an increasing speed up to 6 m/yr in 1987 (Follacci, 1999). All morphological features mapped are then a combination of pre-existing discontinuities and gravitational features induced by the sliding movement.

The landslide can be divided in to four distinct parts (Figure 2), these distinctions were made by comparing aerial photographs (1974, 1991, 1995, 1999, 2004) from the Institut Geographique National (IGN) database, measured and calculated displacement rates (Follacci, 1999; Serratrice, 2001; Casson *et al.*, 2005) and field investigations.

The first part was the first area showing signs of destabilization in the 1950s. The first recorded evidence of failure is a N175 motion that is structurally guided by the geometrical relations between the F2-3-4 and FA faults and the lower boundary of the toppled zone (Figure 2). The failure propagation showed an upward progression close to the FA fault that corresponds to the first sliding unit. The failure surface is about 100 m deep (Figure 3), which seems to be the deepest part of the overall landslide; this is in agreement with the model proposed by Gugliemi *et al.* (2005). The movement is a combination of complex overlapping failures guided by the faults F2-3-4 that are described by the orientations of the morphological features. Current movements are influenced by the overall mass. The sliding direction has reoriented to a N220 motion characterized by scarps having a N120 orientation and the development of more superficial movements as rock falls near blocky areas and retrogressive superficial landslides corresponding to scree reactivation and circular failures near the foot of the slope.

The second part of the structure of the landslide was first induced by movements linked to the F2 orientation (Figures 2 and 3). However, most directions in this part highlight a N220 motion and the development of superficial block collapse as screes and superficial slides. The movement does not reach the toppled zone as it does not mobilize pre-existing trenches. The sliding surface in this zone remains very superficial and seems to have appeared more recently as a consequence of the movement of the remaining slope.

The third part shows also the combination of two movement directions (Figure 2). The first one is mostly located between faults F2-3 and is linked to the movement of part one. A second major orientation has a N120 direction due to a downward N220 motion. This downward movement is characterized by scarps in the lower part due to readjustments after destabilization respectively of parts one and two. Deformation mainly consists of traction-opening of trenches with a high deformation rate in the south-eastern part. Failure propagation at the base of those trenches followed a N40 direction with an upward propagation of the landslide over time up to the FB fault that bound today's unstable zone. High deformation rates in this unstable zone allowed the initiation of a superimposed blocky landslide (Figure 3) which is currently the most active part of the overall landslide (Casson *et al.*, 2005, Jomard *et al.*, 2007a).

The fourth part is a relatively stable area (Figure 2). Pre-existing trenches show small deformations compared to the overall sliding zone. Movements are bounded to a N220 motion with a deformation by toppling leading to rock falls. It could mean that the failure surface has not yet completely propagated under this zone.

Deformation and the increasing number of trenches above and in the western boundaries of the sliding zone are significant and would probably induce a future extension of the landslide westward and up to the FC fault as a next step.

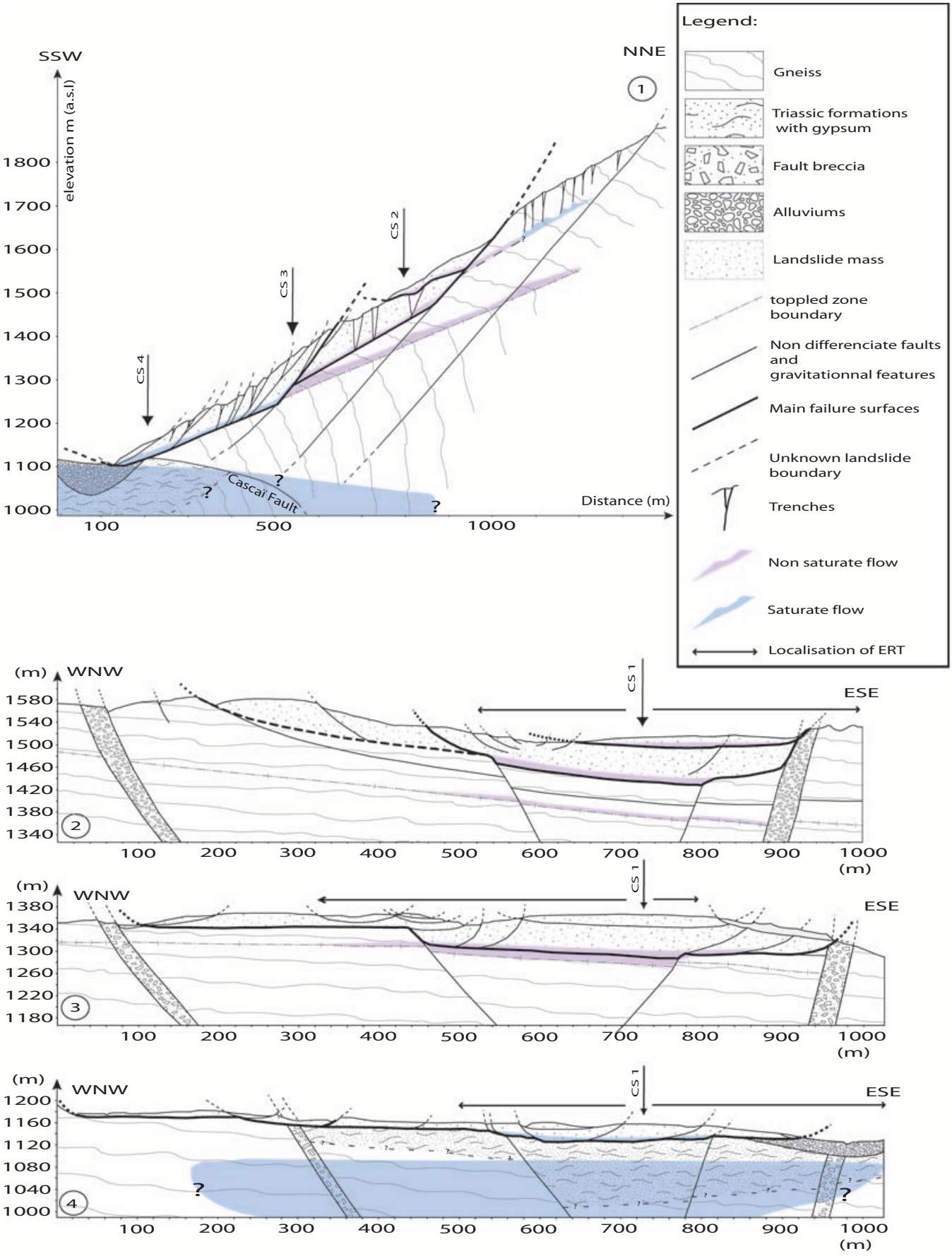

Figure 3. Geological cross-section of the La Clapière slope. Both landslide morphology and water repartition are complex with a predominant structural control. An upward extension of the landslide will develop according to a retrogressive failure mechanism. This figure is available in colour online at www.interscience.wiley.com/journal/espl

Although only aerial views are available to confirm the described movements from the 1950s to the end of the 1970s, displacement measurements and accurate photogrammetric views of the landslide made by the French Ministry of Equipment services have been available since the beginning of the 1980s (Follacci *et al.*, 1987). Mean displacement of the landslide between 1982 and 1986 was 13·3 m. The motion peaked at 80 mm/day during a three month period in summer 1987. Quantitative comparisons between 1983 and 1999 photogrammetric views (Casson *et al.*, 2003) have allowed the total displacement of several landmarks to be determined. A downward progression of 115 m of the landslide front which correspond to a globally constant rate of 1·7 cm/day. This deformation rate is comparable with the average rate determined for the whole rockslide body (1·7 cm/day, Casson *et al.*, 2003). But, taking into account the highlighted rockslide parts, deformation rates of some landmarks are more heterogeneous within the landslide body (Casson *et al.*, 2003): a 100 m displacement in part one (1·47 cm/day); 160 m in part two (2·36 cm/day); 120 m in part three (1·67 cm/day); and a retreat of the north-eastern head-scarp of about 260 m (4·1 cm/day) showing the upward propagation of the rupture up to the FB fault. These motions have a relatively homogeneous N220 direction (Casson *et al.*, 2005) showing a global deformation of the overall mass. However, the differences in the range of deformation rates is a significant sign supporting the existence of the described compartments and their geomorphological representation.

From a hydrogeological point of view, many studies have been conducted (Compagnon *et al.*, 1997, Guglielmi *et al.*, 2000, Cappa *et al.*, 2004) giving details to understand and represent water in cross-sections (Figure 3). The landslide can be divided into a higher part with unsaturated water circulation on the sliding surface and a saturated lower part. This difference may have been a critical factor for the destabilization of the landslide base. Deep water tables are also represented corresponding to the foot of the toppled zone in the higher slope part and to the basal aquifer (Cappa *et al.*, 2004).

Electrical Resistivity Tomography (ERT)

Protocol used for ERT

The protocol used for this study was previously tested in Jomard *et al.* (2007a) giving accurate results in the higher part of the landslide. The same protocol has been followed in this study. The key acquisition and inversion parameters are described later.

Measurements were undertaken with a multielectrode 2D device, using the Syscal R1 Plus imaging system (IRIS Instrument). The 2D devices are composed of 48 electrodes separated by 10 m (limit of the system). ERT1 and ERT2 making a total length of 480 m. An overlapping of 50% was made for the ERT3 which is a combination of two profiles in order to extend the profile over a length of more than 500 m and cross some expected major structures. Pole-pole and dipole-dipole arrays have been acquired for each profile (ERT1-2-3). Each acquisition point is stacked three to five times and the obtained value is deleted if the quality factor (corresponding to a deviation between the injected power and received signal) is not null. For pole-pole arrays, the location of infinite electrodes has been done with respect to recommendations mentioned in Robain *et al.* (1999). In particular, infinite electrodes are placed symmetrically on both sides of the in-line electrodes with a spread angle of more than 30°. However, the length of 'infinite lines' does not reach more than 7 to 10 times the greatest 'in-line' electrode distance because of problems introduced by the shape of this mountainous steep terrain. This limitation can introduce an almost homogeneous under evaluation of the deepest measurements as proposed by Robain *et al.* (1999). This problem is partly addressed by the very consistent correlation observed between resistivity ranges obtained for dipole-dipole and pole-pole arrays in our previous work (Jomard *et al.*, 2007a).

In this paper, the ERT presented are only for pole-pole arrays, because other configurations could not penetrate to the 100 m depth assumed for the failure surface (Jomard *et al.*, 2007a). The resolution of the acquired profiles is a function of the number of acquisition points; a grid of about 10 × 10 (in metres) was created in agreement with the geological settings scale. It corresponds to about 1000 measurement points for each ERT and should allow probing theoretically down to a 250 m calculated depth (Edwards, 1977).

Inversion of the data is then required to obtain a vertical true resistivity section through the underlying structure (Loke and Barker, 1996). The field data were inverted with software RES_{2D}INV written by Loke (1997). Constraints provided by the topographic variations have been incorporated in the inversion processing. The results of the inversion process are presented in Figures 4–6. The resolution obtained through the inversion process is presented in Figure 4, this resolution is acceptable in comparison with geological parameters presented in the cross-sections (Figure 3) and the continuous pseudo-section (Figure 4).

Analyses and discussion of field measurements

All figures presented in this paragraph are the resistivity models resulting from inversions with RES_{2D}inv software (Loke, 1997).

According to the relative basement homogeneity for ERT1 and ERT2 (Figure 3), we will be able to associate resistivity contrasts not to the lithological variations, but to the coupling between rocks mechanical weathering, saturation and fracturing. In general, resistivity variations can be explained by (Jongmans and Garambois, 2007):

- The water content. In the same geological formation resistivity variation is a function of the ratio saturation/porosity of the rock.
- The rock weathering. It can be considered two ways: chemical weathering and mechanical weathering. Chemical (hydrolysis) weathering induces an increase content of clay and the decreasing of the permeability. Mechanical weathering followed by gravitational movements induces a porosity increasing in a destructured medium. Both weathering types are characterized by a resistivity increase

ERT 3 will also be dependent to lithological variations at depth (Figure 3).

ERT descriptions

ERT1 (Figure 4) presents a very large resistivity variability from 50 Ω m to 7000 Ω m and a relatively low misfit of 13%. It highlights a vertical distribution in three main zones: two conducting zones located at depth and near the surface (first and third bodies, Figure 4), separated by a more resistant one. The lower zone (<500 Ω m) and the resistant one (2000 to 7000 Ω m) are separated by a boundary of clear resistivity contrast located at a depth of 110–150 m. The resistant body is characterized by heterogeneous resistivities with an undulated representation in the shape of bulbs with a resistant core.

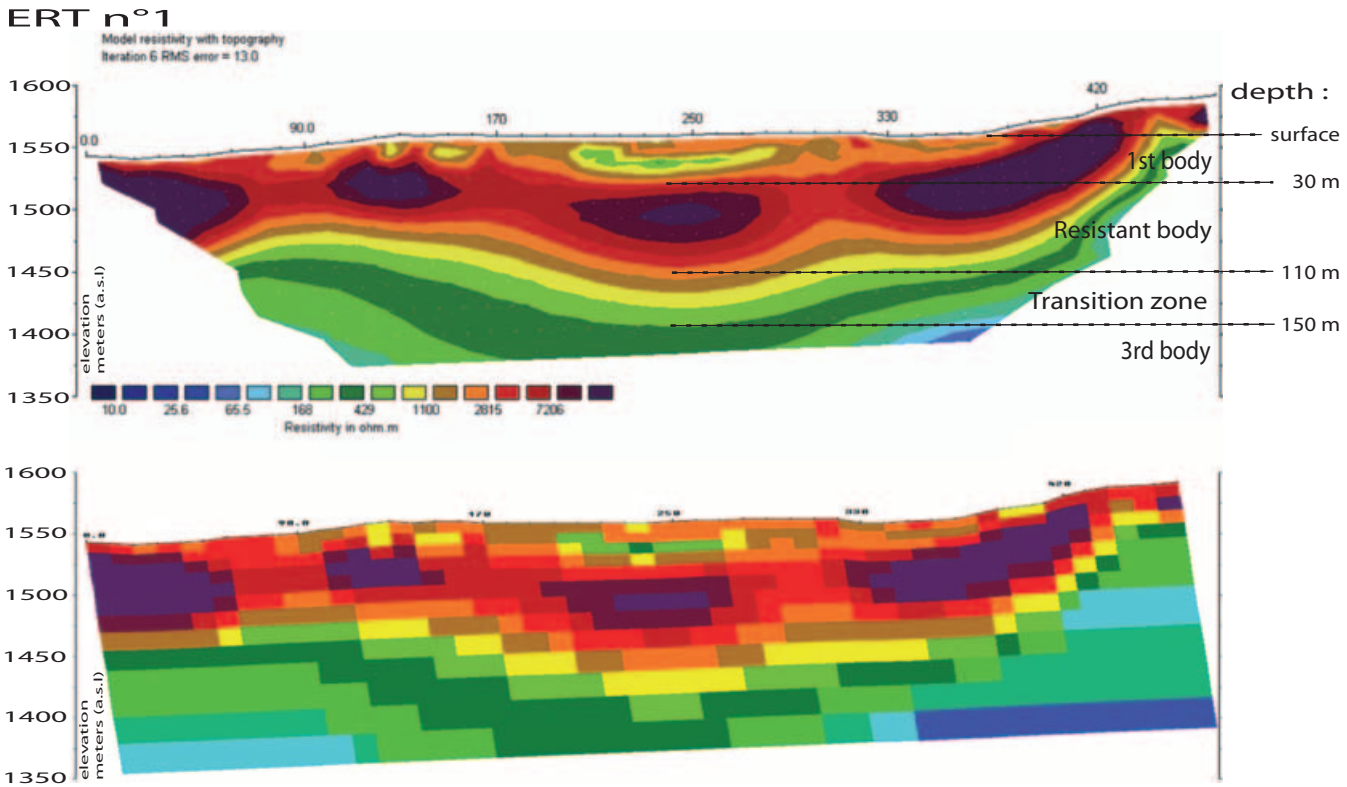

Figure 4. Electrical Resistivity Tomography number one (ERT1). This inversion model including topography presents three near horizontal distinct resistive layers, a resistant undulated body surrounded by two more conductive ones. The major limits are indicated for Figures 4–6 with their depth relative to the topographic surface; the resistivity scales are also homogenized for the three profiles. Calculated cells are represented on the second profile showing the resolution and the accuracy of the inversion process (which is equivalent for ERT2 and ERT3). This figure is available in colour online at www.interscience.wiley.com/journal/espl

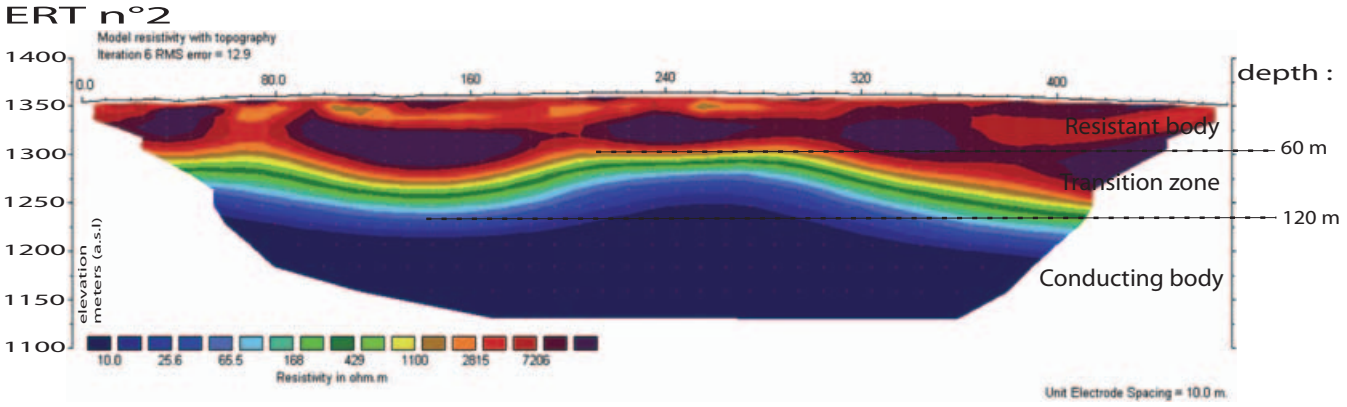

Figure 5. Electrical Resistivity Tomography number two (ERT2). This inversion model presents two near horizontal distinct resistive layers. A resistant undulated body lay over a conductive one. This figure is available in colour online at www.interscience.wiley.com/journal/espl

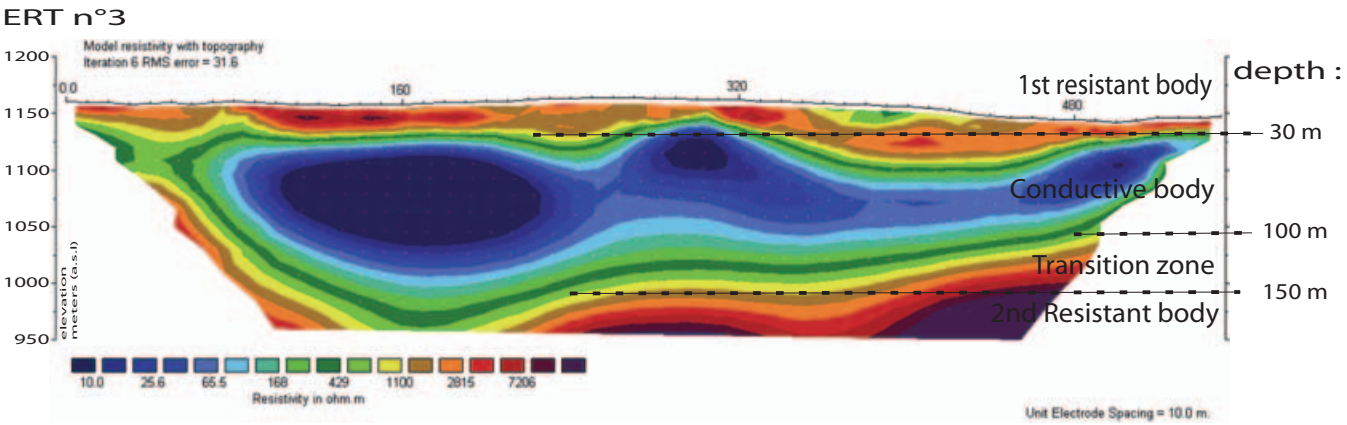

Figure 6. Electrical Resistivity Tomography number three (ERT3). This inversion model presents three near horizontal distinct resistive layers. A conductive body surrounded by two resistant bodies. This figure is available in colour online at www.interscience.wiley.com/journal/espl

The transition between these resistive cores corresponds to linear resistivity reductions from >7000 Ω m to 2800 Ω m. The more superficial third zone presents another resistivity decrease to a mean value of 1500 Ω m with a clear contrast at a depth of 30 m.

ERT2 (Figure 5) highlights shapes and ranges of resistivity comparable to ERT1, excepting the superficial resistivity decrease. The misfit is also comparable with a value 12·9%. Both resistivity bodies are more homogeneous compared to ERT1. The more resistant one still presents an undulated shape with resistant cores and the lower one is characterized by a mean lower resistivity value (20 Ω m). Moreover, the resistivity contrast between the two bodies (and then between ERT1 and ERT2) is more important and corresponds to a depth varying from 60 to 120 m.

ERT3 (Figure 6) presents a different shape compared to ERT1 and ERT2 below a depth of 150 m. The misfit is high compared to the precedent profiles (31·6%). A second resistant body can be distinguished under the conducting mass. However, the transition between conductive and resistant zones is characterized by high resistivity contrasts (as observed on ERT2) and located respectively at depths of 30 m and 100–150 m.

Comparison with geologic profiles (Figure 7)

The three acquired profiles (ERT1–3) are compared with the geological interpretation of the landslide previously drawn on the same transects (Figure 7).

For ERT1, a globally high correlation between the subsurface structure and electrical information can be observed. From the surface to the depth, the conducting superficial body corresponds well to the superficial secondary landslide as shown and discussed by Jomard *et al.* (2007a). The main landslide body is characterized by the resistive part which could be associated with a highly deformed and destructured unsaturated mass. The depth of the interpreted sliding surface is well represented at a depth at about 80/90 m. At this altitude, the sliding surface is considered to be characterized by an unsaturated flow which can explain the drop of resistivity with a lower contrast compared to ERT2. The extreme lower zone corresponds to the toppled limit depth represented by a saturate flow zone that explains the continuous resistivity decrease down to values lower than 100 Ω m.

ERT2 can be interpreted in an equivalent form. From surface to the depth, the first body observed in ERT1 is not represented any more. This difference can be explained by the absence of overlapping landslide draining superficial water in this part of the La Clapière rockslide. Below, the transition gradient between the two resistivity bodies is more abrupt compared to ERT1 and is located at a mean depth consistent with the geological interpretation (90 m). This strongest gradient can be explained by the influence of a water content increase through the sliding surface. Indeed, the sliding surface zone is characterized in this landslide part by a saturate water flow that should introduce a higher electric contrast than in the ERT1 case. From this transition zone to the base of the profile, resistivities are quite homogeneous (<50 Ω m), which is a problem in comparison with the geological cross-section where the lowest part is not recognized as a saturated zone. A strong influence of water content on acquired resistivities at

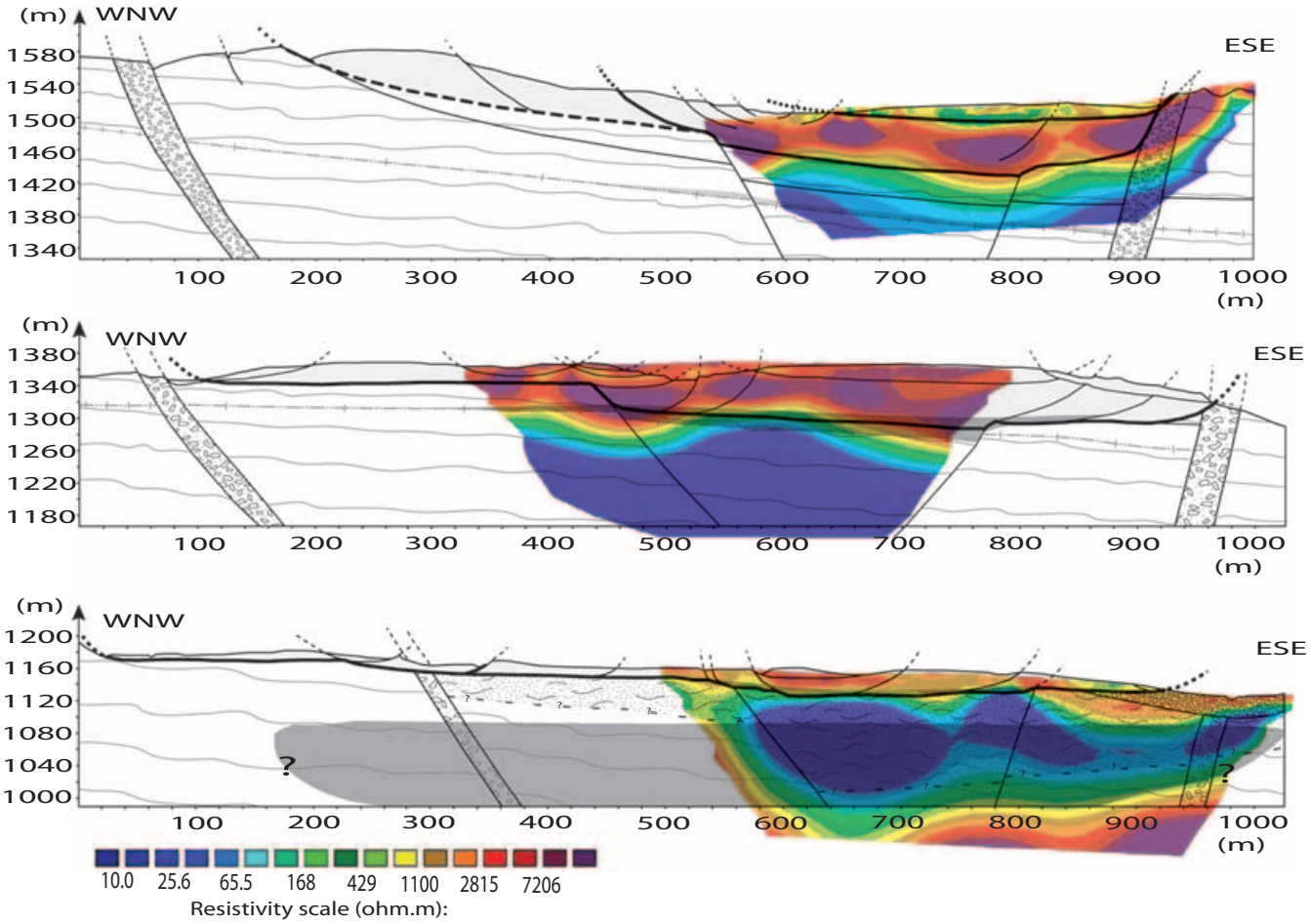

Figure 7. ERT projections on geological cross-sections. It highlights a good correlation with sub-horizontal structures although vertical features are not well explained. This figure is available in colour online at www.interscience.wiley.com/journal/espl

depth, introduced by the saturated sliding surface level and/or through draining vertical faults, playing as a short cut for current lines propagation could be a way to explain this observation.

ERT3 was made on a much more heterogeneous geological structure. The upper resistant body, corresponding to the destructured media of the landslide mass is still coherent with the geological cross-section. The brutal transition to lower resistivities (<50 Ω m) at a depth of about 30 m corresponds to the combination of the saturated sliding surface and the underlying water table affecting Triassic deposits. This conducting zone is thicker in the west-northwest (WNW) part of the profile, consistent with the localization of the Triassic formation maximum thickness. Finally, the deep resistivity increase could be associated with the unsaturated metamorphic basement under the Cascaï overthrusting fault (Figure 3).

The comparison between electrical profiles and geological cross-sections indicates that the horizontal geological structures are well correlated and reproduced by electrical tomography for the three profiles. In particular, the precision of their localization at depth seems to be accurate at this survey scale. On the contrary, the representation of vertical structures such as faults is not directly observable with the pole-pole geophysical surveys; but the undulated interface between resistant/conductive bodies and the bulb and core heterogeneity within the undulating resistant body observed on the three acquired electric profiles cannot be adequately explained with only horizontal heterogeneities. It can be observed, especially in ERT1 and ERT2, that the electrical undulations are present where vertical geological discontinuities have been mapped. This observation implies that vertical structures could have an influence in the acquired profiles. Therefore simplistic models were made to estimate the signature of vertical structures in the acquired profile inversions.

Resistivity modelling (Figure 8)

Resistivity modelling was conducted to assess the reliability of the information obtained from ERT pole-pole profiles. Two main problems rose from their analysis:

- The estimation of the signal induced by the presence of vertical heterogeneities,
- The influence of geological complexity to explain the increasing misfit between the three acquired profiles.

The Res_{2D}mod software (Loke, 2002) was used for this resistivity modelling. Models are computed by (i) the integration of a determined 2D geometry divided in resistivity bodies, and (ii) a forward-calculation process depending on the survey configuration.

The models presented in this paper were tested with geometries in agreement with the field profiles: an electrode spacing of 10 m, a total length of about 500 m, a pole-pole configuration, an investigation depth around 300 m. From there, three models were computed taking into account three imposed geometries corresponding to field analysis and presenting an increasing complexity:

- A two parallel layer model to represent the interface between the landslide mass and the stable area taking into account a clear transition zone at a depth of 80 m.
- A two parallel layer model with the same characteristics and the adjunction of four vertical faults. Faults are represented by a thin zone of about 10 m. Faults are irregularly distributed along the profile to test the accuracy of the localization; lateral spacing between them is more than 100 m.
- A two parallel layer model with four dipping faults. A dipping angle consistent with angles observed on the field is introduced to the precedent faults.

A range of three characteristic resistivities were attributed to these different bodies for modelling: (i) a conducting basal layer (50 Ω m) representing the saturated stable bedrock; (ii) a resistant upper layer (5000 Ω m), which represent the landslide body with weathered and destructured gneisses on a 80 m thickness; (iii) an intermediate 250 Ω m. value for the representation of faults. Those resistivities were determined by analysis performed on rock samples by Lebourg *et al.* (2005).

Two parallel layer model (Figure 8a)

The calculated resistivity model (Figure 8a) well reproduces the imposed geometry. The error on the interface depth localization (80 m) and the introduced resistivities is negligible. Furthermore the calculated root mean square (RMS) (4·8%) is very low compared to the field profiles.

Two parallel layer model with vertical faults (Figure 8b)

Forward-calculation with faults introduces strong heterogeneities but the vertical signature of faults is not reproduced. In detail, the interface depth is still well reproduced around 80 m but appears strongly undulated. The resistivity contrast between the two principal bodies is enhanced. In addition, the shape of the resistive body presents strong lateral variations in the form of cores separated by the concentration of nodes of less important resistivities localized on the introduced fault zones. The resistivity of the conductive body is over evaluated of a ratio of 10. The calculated RMS increases up to 16·6% with the integration of faults.

Two parallel layer model with dipping faults (Figure 8c)

The introduction of dipping faults with a dip of 70° (Figure 8c) does not fundamentally modify the precedent results (Figure 8b). However the following points can be seen: (i) the interface undulation is smoothed when the faults dips increase and the interface at 80 m seems to be under evaluated (10%) because of a less clear transition, (ii) lateral heterogeneities are enhanced and (iii) the RMS increases to 40·0%.

Model comparison with ERT2 profile (Figure 8d)

Results are compared to the ERT2 profile. This profile was selected because it showed better contrasts, the best resistivities homogeneity and a good accordance with the geological cross-section. Furthermore, it was acquired on the part of the landslide that seems to present the simplest structure from a geological point of view.

- Comparison of ERT2 with the first model is fairly accurate. The strong resistivity gradient is comparable although the interface is not undulating and the two bodies are quite homogeneous.
- Models b and c are quite similar in their forms (Figure 8d), the introduction of vertical heterogeneities in calculated models correctly reproduced the undulating surface between the two bodies and also the formation of resistivity bulbs in the upper body. Both signs expressed in the ERT2 could then be the expression of vertical heterogeneities in nature. It also seems that a smooth undulation of the transitional zone, observed in ERT2, could be a sign of dipping vertical heterogeneities. The most important result is that the introduction of vertical heterogeneities does not seem to strongly influence the horizontal interface localization at 80 m which confirms the reliability of the profiles for the detection of the sliding surface and associated fluids.

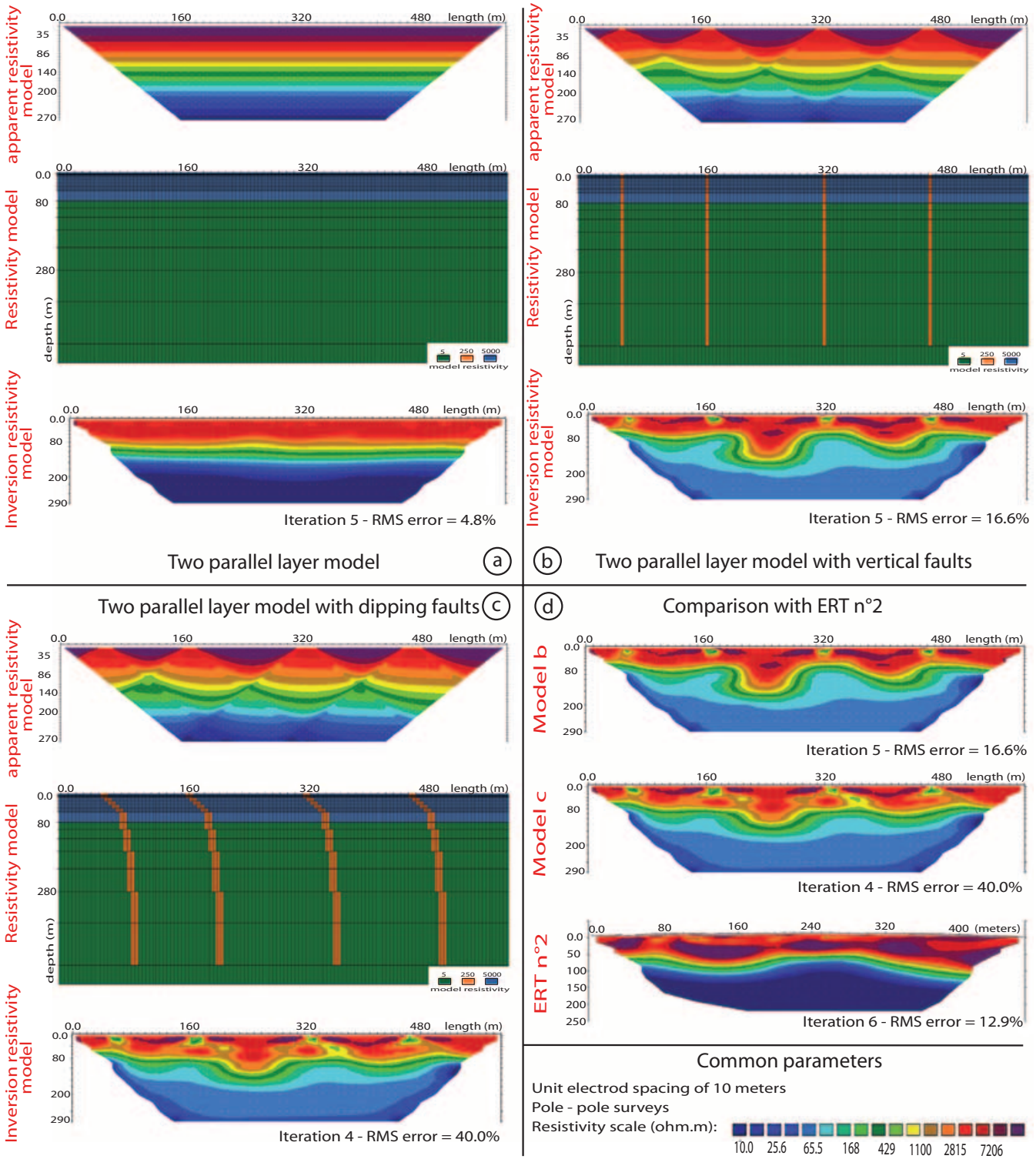

Figure 8. (a) Geoelectrical model a (with the calculated apparent resistivity model, the resistivity model, and the inverse resistivity model section calculated); (b) geoelectrical model b with two layers and four vertical faults; (c) geoelectrical model c with two layers and four dipping faults; (d) comparison between model b, model c and the field ERT2. This figure is available in colour online at www.interscience.wiley.com/journal/espl

However, the calculated lower body is not consistent with the one obtained in ERT2 (a ratio of 10 is observed between models and ERT2). This could be partly explained by the saturation that must homogenize the basement and faults resistivities, especially because faults are often recognized as drains for groundwater alimentation (Cappa *et al.*, 2004; Guglielmi *et al.*, 2005; Lebourg *et al.*, 2005; Jomard *et al.*, 2007a, Jomard *et al.*, 2007b).

Furthermore, the variation of the misfit in models a, b and c clearly shows that increasing the geological complexity will strongly influence the results of ERT tomography. This should be taken into account before underestimating the reliability of ERT and be further developed in the future. In the case of La Clapière the high misfits obtained should therefore be a sign of structure complexity, in particular for the ERT3 (Figure 7).

Conclusion

The synthesis of 25 years of observations and analysis on the La Clapière landslide coupled with an accurate morphological and geological mapping allowed the creation of a better and updated structural map and geological cross-sections including hydrological water flow paths in and around the landslide. The final landslide body structure results from a complex inherited slope structure which strongly guides local deformation and long-term evolution. It results in a complex morphology of the sliding surface which should be later integrated for numerical and physical modelling.

Moreover, electrical tomography was, for the first time, successfully conducted on a deep seated landslide. Results obtained with this method (pole-pole survey) at this scale are accurate to define horizontal heterogeneities of slopes, in particular those introduced by water circulation and porosity/dislocation of geologic materials. Indeed, correlations with field analyses confirm the localization of the reconstructed sliding zone at expected depths (down to an 80–100 m depth). It also confirms hydrological models previously drawn by Cappa *et al.* (2004) and Gugliemi *et al.* (2005). On the contrary, vertical structures are poorly reproduced with this kind of electrical survey, but it is clear that the signal still contains information that can be explored to confirm field hypothesis. ERT therefore provides an efficient geophysical tool for preliminary studies on deep seated landslides by giving quickly good constraints on their internal structures.

Further studies using much longer and precise devices coupled with the development of more powerful and adaptive modelling tools are the next steps in developing the use of geoelectrical tomography on steep and irregular destabilized rock slopes. Comparisons in other well known cases of deep seated landslides such as the Séchilienne landslide (Meric *et al.*, 2005) or the Rosone slope (Binet *et al.*, 2007) should also be conducted in order to validate the methodology at this scale.

Acknowledgements—This work was supported by the PACA Region. Authors would like to acknowledge Professor D. Nobes for his constructive remarks and English corrections.

References

Agnesi V, Camarda M, Conoscenti C, Di Maggio C, Diliberto IS, Madonia P, Rotigliano E. 2005. A multidisciplinary approach to the evaluation of the mechanism that triggerd the Cerda landslide (Sicily, Italy). *Geomorphology* **65**: 101–116.

Ayalew L, Yamagishi H, Marui H, Kanno T. 2005. Landslides in Sado Island of Japan: Part I. Case studies, monitoring techniques and environmental considerations. *Engineering Geology* **81**: 419–431.

Benderitter Y, Schott JJ. 1999. Short time variation of the resistivity in an unsaturated soil. The relationship with rainfall. *European Journal of Environmental and Engineering Geophysics* **4**: 37–49.

Bichler A, Bobrowsky P, Best M, Douma M, Hunter J, Calvert T, Burns R. 2004. Three-dimensional mapping of a landslide using a multigeophysical approach: the Quesnel Forks landslide. *Landslides* **1**: 29–40.

Binet S, Mudry J, Scavia C, Campus S, Bertrand C, Guglielmi Y. 2007. In situ characterization of flows in a fractured unstable slope. *Geomorphology* **86**: 193–203.

Bogdanoff S, Ploquin A. 1980. Les gneiss et migmatites du massif de l'Argentera (Alpes-Maritimes): apport de deux coupes géochimiques. *Bulletin de la Société Géologique de France* **29**: 353–358.

Bogoslowsky VA, Ogilvy AA. 1977. Geophysical methods for the investigation of landslides. *Geophysics* **42**: 562–571.

Brueckl E, Parotidis M. 2001. Estimation of large-scale mechanical properties of a large landslide on the basis of seismic results. *International Journal of Rock Mechanics and Mining Sciences* **38**: 877–883.

Bruno F, Marillier F. 2000. Test of high-resolution seismic reflection and other geophysical techniques on the Boup landslide in the Swiss Alps. *Surveys in Geophysics* **21**: 333–348.

Cappa F, Guglielmi Y, Soukatchoff VM, Mudry J, Bertrand C, Charmoille A. 2004. Hydromechanical modeling of a large moving rock slope inferred from slope levelling coupled to spring long-term hydrochemical monitoring: example of the La Clapière landslide (Southern Alps, France). *Journal of Hydrology* **291**: 67–90.

Caputo R, Piscitelli S, Oliveto A, Rizzo E, Lapenna V. 2003. The use of electrical resistivity tomographies in active tectonics: examples from the Tyrnavos basin, Greece. *Journal of Geodynamics* **36**: 19–35.

Caris JPT, Van Asch ThWJ. 1991. Geophysical, geotechnical and hydrological investigations of a small landslide in the French Alps. *Engineering Geology* **31**: 249–276.

Casson B, Delacourt C, Baratoux D, Allemand P. 2003. Seventeen years of the 'la Clapière' landslide evolution analysed from orthorectified aerial photographs. *Engineering Geology* **68**: 123–139.

Casson B, Delacourt C, Allemand P. 2005. Contribution of multitemporal remote sensing images to characterize landslide slip surface – application to the La Clapière landslide (France). *Natural Hazards and Earth System Sciences* **5**: 425–437.

Colella A, Lapenna V, Rizzo E. 2004. High-resolution imaging of the High Agri Valley Basin (Southern Italy) with electrical resistivity tomography. *Tectonophysics* **386**: 29–40.

Compagnon F, Guglielmi Y, Folacci JP, Ivaldi JP. 1997. Approche chimique et isotopisque de l'origine des eaux en transit dans un grand mouvement de terrain: exemple du glissement de la Clapière (Alpes Maritimes, France). *Compte Rendu de l'Académie des Sciences* **325**: 565–570.

Edwards LS. 1977. A modified pseudosection for resistivity and IP. *Geophysics* **42**: 1020–1036.

Fabbri O, Cappa F. 2001. Apports de l'analyse structurale à la compréhension de la dégradation du glissement de la Clapière, Massif du Mercantour, Alpes Maritimes. Séance Spécialisée de la Société Géologique de France: Hydrogéochimie et hydrodynamique des fluides lieés aux déformations de la croûte supérieure. Besançon, 13–14.

Faure-Muret A. 1947. Sur des affleurements de Trias pincés dans les schistes cristallins de la vallée de la Tinée (Alpes-Maritimes). *Compte Rendu de l'Académie des Sciences* **224**: 205–207.

Ferrucci F, Amelio M, Sorriso-Valvo M, Tansi C. 2000. Seismic prospecting of a slope affected by deep-seated gravitational slope deformation: the Lago Sackung, Calabria, Italy. *Engineering Geology* **57**: 53–64.

Follacci JP. 1987. Les mouvements du versant de la Clapière à Saint-Etienne-de-Tinée (Alpes Maritimes). *Bulletin des Laboratoires des Ponts et Chaussées* **150–151**: 39–54.

Follacci JP. 1999. Seize ans de surveillance du glissement de la Clapière (Alpes Maritimes): *Bulletin des Laboratoires des Ponts et Chaussées* **220**: 33–51.

Follacci JP, Guardia P, Ivaldi JP. 1988. Le Glissement de la Clapière (Alpes Maritimes, France) dans son cadre géodynamique, in *Landslides*, C. Bonnard (ed.). Balkema: Rotterdam; 1323–1327.

Forlati F, Gioda G, Scavia C. 2001. Finite element analysis of a deep-seated slope deformation. *Rock Mechanics and Rock Engineering* **34**: 135–159.

Garambois S, Sénéchal P, Perroud H. 2002. On the use of combined geophysical methods to assess water content and water conductivity of near-surface formations. *Journal of Hydrology* **259**: 32–48.

Godio A, Bottino G. 2001 Electrical and electromagnetic investigation for landslide characterisation. *Physics and Chemistry of the Earth* **26**: 705–710.

Godio A, Strobbia C, De Bacco G. 2006. Geophysical characterisation of a landslide in an alpine region. *Engineering Geology* **83**(1–3): 273–286.

Gourry J-C, Vermeersch F, Garcin M, Giot D. 2003. Contribution of geophysics to the study of alluvial deposits: a case study in the Val d'Avaray area of the River Loire, France. *Journal of Applied Geophysics* **54**: 35–49.

Griffiths DH, Turnbull J. 1985. A multi-electrode array for resistivity surveying. *First Break* **3**: 16–20.

Griffiths DH, Barker RD. 1993. Two-dimensional resistivity imaging and modelling in areas of complex geology. *Journal of Applied Geophysics* **29**: 211–226.

Guglielmi Y, Bertrand C, Compagnon F, Follacci JP, Mudry J. 2000. Acquisition of water chemistry in a mobile fissured basement massif: its role in the hydrogeological knowledge of the La Clapière landslide (Mercantour massif, Southern Alps, France). *Journal of Hydrology* **229**: 138–148.

Guglielmi Y, Cappa F, Binet S. 2005. Coupling between hydrogeology and deformation of mountainous rock slopes: insights from La Clapière area (Southern Alps, France). *Comptes Rendus Geosciences* **337**: 1154–1163.

Gunzburger Y, Laumonier B. 2002. Origine tectonique du pli supportant le glissement de terrain de la Clapière (Nord-Ouest du massif de l'Argentera-Mercantour, Alpes du Sud, France) d'apres l'analyse de la fracturation: a tectonic origin for the fold underlying the Clapière landslide (NW Argentera-Mercantour massif, Southern Alps, France) deduced from an analysis of fractures. *Comptes Rendus Geosciences* **334**: 415–422.

Hack R. 2000. Geophysics for slope stability. *Surveys in Geophysics* **21**: 423–448.

Hutchinson JF. 1983. Methods of locating slip surfaces in landslides. *Bulletin of the Association of Engineering Geologists* **XX**: 235–252.

Israil M, Pachauri AK. Geophysical characterization of a landslide site in the Himalayan foothill region. *Journal of Asian Earth Sciences* **22**: 253–263.

Ivaldi JP, Guardia P, Follacci JP, Terramorsi S. 1991. Plis de couverture en échelon et failles de second ordre associés à un décrochement dextre de socle sur le bord nord-ouest de l'Argentera (Alpes-Maritimes, France). *Comptes Rendus de l'Académie des Sciences Paris* **313**: 361–368.

Jomard H, Lebourg T, Tric E. 2007a. Identification of the gravitational boundary in weathered gneiss by geophysical survey: La Clapière landslide (France). *Journal of Applied Geophysics* **62**: 47–57.

Jomard H, Lebourg T, Binet S, Tric E, Hernandez M. 2007b. Characterization of an internal slope movement structure by hydrogeophysical surveying. *Terra Nova* **19**(1): 48–57.

Jongmans D, Garambois S. 2007. Geophysical investigation of landslides: a review. *Bulletin de la Société Géologique de France* **178**(2): 101–112.

Julian M, Anthony E. 1996. Aspects of landslide activity in the Mercantour Massif and the French riviera, southeastern France. *Geomorphology* **15**: 275–289.

Lapenna V, Lorenzo P, Perrone A, Piscitelli S. 2003. High resolution geoelectrical tomographies in the study of Giarrossa Landslide (Southern Italy). *Bulletin of Engineering Geology and the Environment* **62**: 259–268, 2003.

Lebourg T, Frappa M. Mesures géophysiques pour l'analyse des glissements de terrain. *Revue Française de Géotechnique* **96**: 33–40.

Lebourg T, Binet S, Tric E, Jomard H, El bedoui S. 2005. Geophysical survey to estimate the 3D sliding surface and the 4D evolution of the water pressure on part of a deep seated landslide. *Terra Nova* **17**: 399–407.

Loke MH. 1997. *Res_{2D}inv Software User's Manual*. http://www.geoelectrical.com/downloads.php

Loke MH. 2002. *Res_{2D}mod, Rapid 2D Resistivity Forward Modelling using Finite-difference and Finite-element Methods. Version 3.01*. 15 pp.

Loke MH, Barker RD. 1996. Rapid least square inversion of apparent resistivity pseudosection by a quasi Newton method. *Geophysical Research Letter* **44**: 131–152.

Malaroda R, Carraro F, Dal Piaz GV, Franceschetti B, Sturani C, Zanella E. 1970. Carta geologica del Massicio dell'Argentera alla scala 1 : 50.000 e Note illustrative. *Memorie della Società Geoligica ITALIANA A* **IX**: 557–663.

Maquaire O, Flageollet JC, Malet JP, Schmutz M, Weber D, Klotz S. 2001. Une approche multidisciplinaire pour la connaissance d'un glissement-coulée dans les marnes noires du Callovo-Oxfordien (Super Sauze, Alpes de Hte Provence, France). *Revue Française de Géotechnique* **95–96**: 15–32.

Mauritsch HJ, Seiberl W, Arndt R, Römer A, Schneiderbauer K, Sendlhofer GP. 2000. Geophysical investigations of large landslides in the carnic region of Southern Austria. *Engineering Geology* **56**: 373–388.

McCann DM, Forster A. Reconnaissance geophysical methods in landslide investigations. *Engineering Geology* **29**: 59–78.

McGrath RJ, Styles P, Thomas E, Neale S. 2002. Integrated high-resolution geophysical investigations as potential tools for water resource investigations in karst terrain. *Environmental Geology* **42**: 552–557.

Meric O, Garambois S, Jongmans D, Whatelet M, Chaltelain JL, Vengeon JM. 2005. Application of geophysical methods for the investigation of the large gravitational mass movement of Séchilienne, France. *Canadian Geotechnical Journal* **42**(4): 1105–1115.

Merrien-Soukatchoff V, Quenot X, Guglielmi Y. 2001. Modélisation par éléments distincts du phénomène de fauchage gravitaire. Application au glissement de la Clapière (Saint-Etienne de Tinée, Alpes Maritimes). *Revue Française de Géotechnique* **95–96**: 133–141.

Robain H, Albouy Y, Dabas M, Descloitres M, Camerlynck C, Mechler P, Tabbagh A. 1999. The location of infinite electrodes in pole–pole electrical surveys: consequences for 2D imaging. *Journal of Applied Geophysics* **41**: 313–333.

Serratrice JF. 2001. Glissement de la Clapière. Comparaison des MNT de 1970 à 1997. *Journées de Mécanique des Sols et des Roches des LPC, Nancy* June: 19.

Storz H, Storz W, Jacobs F. 2000. Electrical resistivity tomography to investigate geological structures of the earth's upper crust. *Geophysical Prospecting* **48**: 455–471.